

Broadband impedance modeling and single bunch instabilities estimations of the advanced light source upgrade project

Dan Wang^{a,*}, Karl Bane^b, Derun Li^a, Tianhuan Luo^a, Olusola Omolayo^a, Gregory Penn^a, Stefano De Santis^a, Christoph Steier^a, Marco Venturini^a

^a Lawrence Berkeley National Laboratory, 1 Cyclotron Rd, Berkeley, 94720, CA, United States

^b SLAC National Accelerator Laboratory, 2575 Sand Hill Rd, Menlo Park, 94025, CA, United States

ARTICLE INFO

Keywords:

Broadband impedance
Impedance modeling
Impedance budget
Pseudo-Green function
Single bunch instability
ALS-U project

ABSTRACT

The Advanced Light Source Upgrade (ALS-U) is a 4th generation diffraction-limited soft x-ray radiation source, consisting of a new accumulator ring (AR) and a new storage ring (SR). In both rings coupling-impedance driven instabilities need careful evaluation to ensure meeting the machine's high-performance goals. This paper presents the workflow followed in building the impedance models and the beam-stability analysis based on those models. We follow the commonly accepted approach of separating the resistive-wall and the geometric parts of the impedance; the former is obtained by analytical formulas, the latter by numerical electro-magnetic codes (primarily CST Studio software) with perfectly-conducting boundary conditions.

Impedance budgets are established and pseudo-Green functions calculated to be used in beam dynamics studies. We also present various ways to cross-check simulation results for reliable impedance modeling. Finally, the crucial single-bunch instability current thresholds for various operation modes are determined and discussed.

1. Introduction

The upgrade of the Advanced Light Source (ALS-U) to a diffraction-limited soft X-ray radiation source with brightness about two orders of magnitude higher than in the existing ALS is currently underway at the Lawrence Berkeley National Laboratory (LBNL). The upgrade entails the replacement of the ALS storage-ring (SR) triple-bend achromat (TBA) with a multi-bend achromat (MBA) lattice and the installation of a new low emittance TBA lattice accumulator ring (AR) [1,2]. The AR is approximately the same size as the SR and shares the same tunnel.

A feature common to all new 4th generation light sources, including the ALS-U, is the narrow vacuum chamber aperture required to accommodate high field-gradient magnets and high-performance insertion devices. Because the beam-coupling impedance tends to scale with some inverse power of the chamber aperture, the new generation machines are intrinsically more sensitive to impedance-driven collective effects [3]. This places particular importance on the need for a detailed and comprehensive modeling of the beam impedance and emphasis on close coordination with vacuum engineers to optimize the design of critical components.

It is well known that significant discrepancies are often found between impedance modeling and beam-based measurements [4–7], although impedance modeling has improved over the years due to advanced simulation capabilities. It is desirable to have accurate

impedance modeling prior to the machine commission, which can be used to predict collective effects in real machines [5,8,9]. We presented the systematic impedance calculation, optimization, consistency check, error analysis, and its application to the analysis of collective effects for the upcoming ALS-U. This work will also serve as a record for cross-checking with future beam-based measurements in ALS-U. It is hoped that this documentation will benefit recently started upgrade projects and those that may come in the future [10].

The focus of this paper is on the broadband impedance and the associated short-range wakefields [11–14]. Sources of broadband impedance may extend over a significant length of beam pipe (resistive wall) or be localized, such as beam position monitors (BPM), RF cavities, pump screens, insertion devices, etc. In addition to inducing instabilities [7,11] the broadband impedance can affect the machine's performance/operation by causing particle losses [15,16] or overheating of vacuum-chamber components [6,7,11].

Our approach is to represent the broadband impedance by a combination of analytical and numerical models. Analytical formulas have been used to describe resistive wall (RW) impedances and to benchmark the numerical calculations of the impedance of select other sources in the appropriate limits. Except for transitions in beam pipe radius, which are simulated in pairs, wake fields of components are calculated individually; cross-talk between elements is not an issue

* Corresponding author.

E-mail address: dwang2@lbl.gov (D. Wang).

for resistive wall, and other contributions are dominated by localized modes. As described in [10], cross-talk may noticeably impact dynamics for 4th generation light sources, but these corrections can be neglected for the purpose of ensuring that the beam parameters are far from any instabilities.

We have compiled impedance-budget surveys for both the SR and the AR based on the nominal bunch length and computed wake potentials with a 1 mm rms length rigid driver bunch to serve as pseudo-Green functions in beam dynamics macro-particle simulations. The numerical models have been based on detailed designs provided by the vacuum engineers and results from our analysis have informed repeated modifications to those designs.

We present results for both the SR and AR. Not surprisingly, impedance effects in the AR are considerably weaker than in the SR, due to the generally simpler vacuum design, relatively large apertures, absence of insertion devices, reduced number of chamber transitions and Non-Evaporable Getters (NEG) coated chambers. Preliminary results have appeared before in [17,18].

The paper is organized as follows. In Section 2 we show the overview of the AR and SR from the standpoint of impedance sources including the vacuum chambers and their main features, as well as the relevant machine parameters for the instability study. In Section 3 we describe the workflow, present the RW model, describe select geometric-impedance sources and show comparisons with analytical formulas, and discuss the “RL” fitting model (where R is the resistance, and L is the inductance) of short-range wake functions [19]. Systematic results for the AR and SR are in Sections 4 and 5 respectively, including beam-dynamics macroparticle simulation studies with *elegant* [20] for various operating modes. Section 6 shows examples of how our impedance considerations have informed the design of select components. Section 7 presents additional cross-checks for the impedance models, and is followed by the conclusions.

2. ALS-U Accumulator Ring (AR) and Storage Ring (SR)

Fig. 1 is an overview of the ALS-U accelerator complex. The SR average current is 500 mA, distributed evenly among the 284 bunches of the beam, consisting of eleven 25- or 26-bunch trains. The harmonic number is $h = 328$. To inject into the small dynamic aperture of the SR, the beam extracted from the booster is first damped in the AR, which is co-located in the storage-ring tunnel along the inner wall. Injection into the SR is on-axis with swap-out of full trains [1,2] taking place about every half-minute. In both rings the design bunch charge, which is most relevant for single-bunch broadband-impedance driven instabilities, is 1.15 nC. For the AR beam, the rms bunch length is $\sigma_z = 5$ mm, and for the SR beam $\sigma_z = 14$ mm.

The vacuum chamber of the AR is relatively simple and made of a single material (stainless steel) except for the dipole vacuum-chamber sections (copper). The aperture in most arc sections is round with 28 mm inner diameter (ID) and round with 47 mm ID in the straight sections. The dipole chamber is elliptical with 14 mm \times 40 mm ID.

The chamber dimensions are much narrower in the SR, as most round chambers in the arcs have 20 mm or 13 mm ID and, as in most 4th generation light sources [21,22], large parts of the chamber are coated with NEG to mitigate the poor vacuum conductance of the small pipes [23].

Copper is used as the base layer for most of the SR chambers to counter the design features that enhance the resistive wall impedance (the small aperture and extensive use of NEG coating, which mainly affects the imaginary part of the impedance [24]).

The vacuum components in the AR (Table 1) are also relatively simple since there are few unique devices. The chamber features are much more complex in the SR (Table 2), where among other components we have the High-order Harmonic Cavities (HHC) and various insertion devices including narrow-gap Elliptically Polarizing Undulators (EPUs), In-Vacuum Undulators (IVU), wiggler, and photon absorbers along the ring.

3. Overview of the broadband impedance modeling

3.1. General workflow for impedance modeling

The general workflow we have followed to build the broadband impedance model is shown in Fig. 2. The main steps are as follows:

1. Acquire the CAD model of the vacuum components and use tables to keep track of the components’ count, design versions, placement within the ring layout, and relevant local lattice parameters. Categorize the vacuum chamber sections for RW calculation by cross-section, aperture, material, etc.
2. Evaluate the RW and geometric impedance:
 - (a) RW: apply analytical formulas;
 - (b) Geometric impedance: import the CAD model to the 3D simulation code CST [25], to solve Maxwell’s equations for the fields excited by a rigid driver bunch with the nominal bunch length. The simulation code output is the wake potential [26] and the impedance obtained by Fourier transform of the wake potential.
3. Calculate impedance budget and pseudo-Green functions:
 - (a) Compile the total impedance budget, based on a nominal-length bunch driver, and rank sources by various metrics (loss factor, kick factor, etc.);
 - (b) Calculate the pseudo-Green functions based on a bunch driver with a length of only 1 mm for individual sources and their total — this covers almost all the frequency information we are concerned about;
 - (c) Perform consistency checks between the wake-potentials determined with the nominal-length bunch driver and the pseudo-Green functions as a way to detect numerical inaccuracies.
4. Perform macroparticle beam-dynamics studies based on the pseudo-Green functions; determine if the impedance budget is acceptable or if further design optimization is needed.

3.2. Resistive wall impedance modeling

Resistive wall impedance is obtained by applying analytical formulas. Numerical tools are not as accurate as the analytical formulas for resistive wall impedance calculations, especially for short bunch lengths. Because the skin depth is much smaller than the structure dimension, computer resources are limited for such cases where dense meshes are required for accurate calculations.

For the purpose of determining the RW impedance, we have classified the chambers by cross-section type and applied the appropriate analytical formulas. In particular:

- Round cross-section chambers (with or without NEG coating): these are the most common chambers in the AR and SR. Assuming a beam pipe of circular cross section with a single layer of coating, the longitudinal and transverse impedance per unit length are calculated with the analytical formulas [24]:

$$Z_{\parallel}(\omega) = \frac{Z_0 \omega}{4\pi bc} [\text{sgn}(\omega) - i] \cdot \frac{\alpha \tanh \left[\frac{1-i \text{sgn}(\omega)}{\delta_1} \Delta \right] + 1}{\delta_1 \cdot \alpha + \tanh \left[\frac{1-i \text{sgn}(\omega)}{\delta_1} \Delta \right]} \quad (1)$$

$$Z_{\perp}(\omega) = \frac{Z_0}{2\pi b^3} [1 - i \text{sgn}(\omega)] \cdot \frac{\alpha \tanh \left[\frac{1-i \text{sgn}(\omega)}{\delta_1} \Delta \right] + 1}{\delta_1 \cdot \alpha + \tanh \left[\frac{1-i \text{sgn}(\omega)}{\delta_1} \Delta \right]} \quad (2)$$

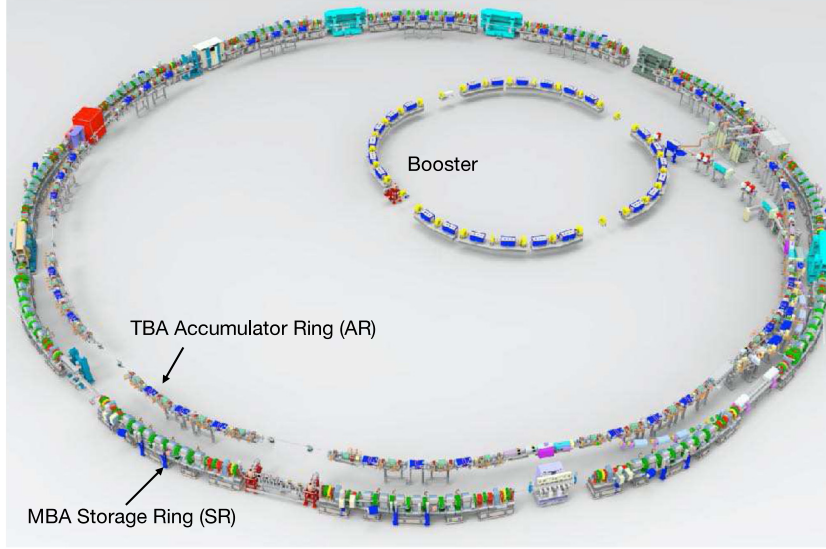


Fig. 1. View of the Advanced Light Source Upgrade (ALS-U) complex.

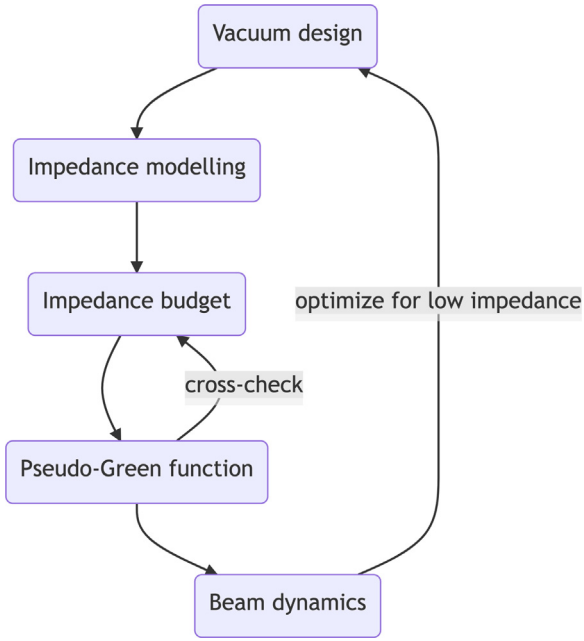


Fig. 2. General workflow to for broadband impedance modeling.

where c is the speed of light, Z_0 is the vacuum impedance, b is the pipe radius, $\sigma_{c,1}$ and $\sigma_{c,2}$ are the material conductivities for the beam pipe and NEG coating respectively, $\delta_1 = \sqrt{2/(\mu_0\sigma_{c,1}|\omega|)}$ is the NEG-coating skin depth and Δ the coating thickness. For a good conductor $\alpha = \delta_1/\delta_2$, with δ_2 being the skin depth of the substrate, assumed to be of infinite thickness. For $\Delta = 0$ the above expressions reduce to the classical DC-conductivity resistive wall impedance formulas [27].

- Elliptical cross-section chambers: they include the chamber for the bend magnet in the AR and the hard-bend chambers in three of the arcs and select insertion device chambers in the SR straight sections. These are modeled using the impedance expressions for a round chamber with radius equal to the minor semi-axis of the ellipse and multiplied by the Yokoya factors (see Appendix A.1) [28]. These depend on the ratio $q = (a-b)/(a+b)$, where a and b are the major and minor elliptical semi-axes. To

a good approximation, the following Yokoya factors apply to all geometries of interest in our case: $F_z \simeq 0.98$ (longitudinal), $F_{d,x} \simeq 0.43$ (horizontal dipole), $F_{d,y} \simeq 0.83$ (vertical dipole), $F_q \simeq 0.4$ (quadrupole; defocusing in the vertical and focusing in horizontal).

- Planar chambers: relevant for some insertion devices such as the in-vacuum undulators (IVU) with parallel plates in the vertical direction, and large open volumes in the horizontal direction. These are modeled using the impedance expressions for the parallel-plate model [29].
- Irregular cross-section chambers. These mainly exist in the SR including chamber sections in the arc with antechambers and key-holes. These are modeled as idealized round or elliptical cross-section chambers, as appropriate. These approximations have been verified with CST simulations using a long bunch driver (rms bunch length 14 mm).

3.3. Geometric impedance modeling

Another important impedance source comes from discontinuities in the ring introduced by components. Selected examples in the SR are shown in Fig. 3, such as flanges with a gasket, button-type beam position monitors together with shielded bellows, gate valves with spring shielding, transition flanges for various insertion devices, photon absorbers, the arc keyhole chambers which each have an opening on its side to let radiation out, the collimators and the RF cavities.

CST Particle Studio is applied to compute the impedance of vacuum chamber components with complex, realistic geometries. Where possible, impedances calculated in CST are compared with analytical formulas used for sections with simple geometry, such as pillbox cavities or step transitions, that approximate the design geometry. A useful collection of these formulas is published in [27]. Typically, agreement is best for low frequencies. Further cross-checks are discussed in Section 7.

RF cavities. Both rings have RF cavities of similar dimensions. A view of the rf cavity in the AR is shown in Fig. 4, which includes the base of the three HOM-dampers in Fig. 4(a) (right), and the reduced model applied in CST in Fig. 4(b) (left), where the radial depth of the cavity is cut at $h \geq 150$ mm, set by $(g + 4\sigma_z)4\sigma_z \leq (h - b)^2$ [30]. This reduced model saves meshes in simulations, which is critical for short bunch calculations, and is valid for short-range wakefield calculations. Unlike the long-range wakefields, short-range wakefields are sensitive only to the environment near the electron beam [27] (where the

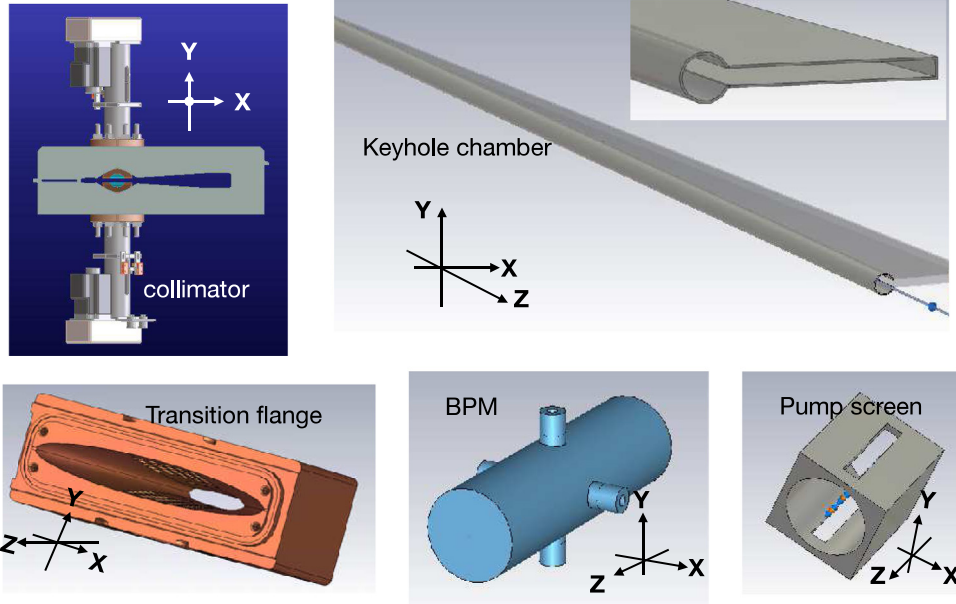


Fig. 3. Examples of various geometric impedance sources in the SR, Z is the beam direction.

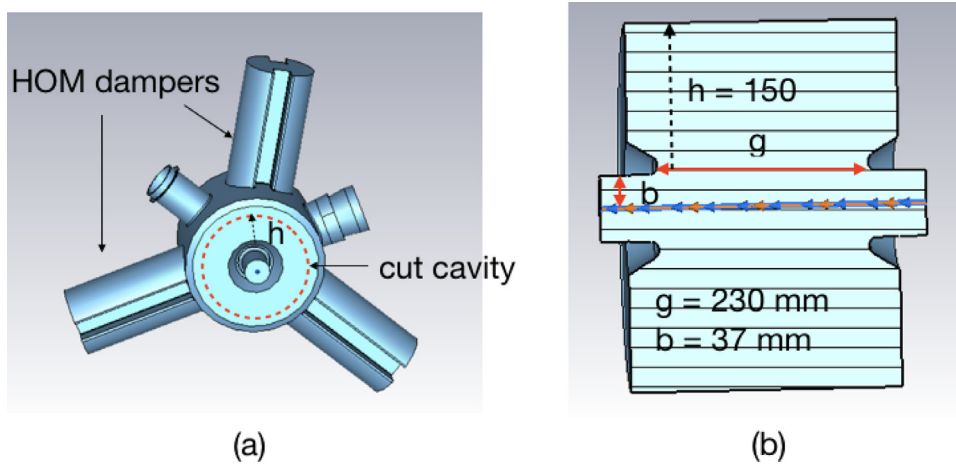


Fig. 4. View of the AR rf cavity including the base of the three HOM dampers (a) and reduced model used for the short-range wake field calculation (b).

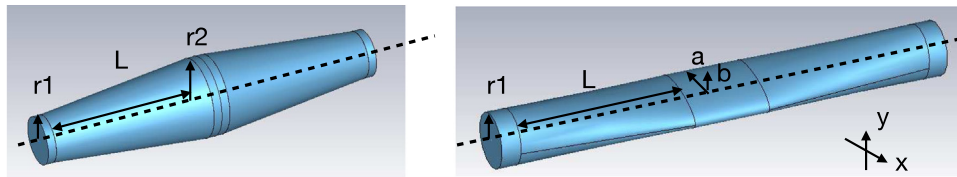


Fig. 5. The two main types of tapered transitions in the AR, left: round transition model, right: elliptical transition model.

reflected RF waves can catch up with particles within the same bunch). CST simulations for a bunch with 5 mm rms bunch length predict a longitudinal loss factor $\kappa_z = 0.98$ V/pC.

Tapered transitions. There are plenty of transitions between different beam pipes in both rings. Transitions turn out to be the largest source of transverse impedance in the AR. In the AR the two prevalent types of transitions are round-to-round and round-to-elliptical (see Fig. 5). Generally, it is preferable to model transitions in pairs (electron beam goes into a narrower/wider region, and then out again) instead of treating each of them separately and then adding the results [31,32]. To minimize computational time, in the numerical model the distance

between the transitions can be taken to be shorter than the physical distance, provided that it remains sufficiently long compared to the aperture. The distance in the numerical simulations is comparable to the taper length. For transitions of the first type (round-to-round), the longitudinal and transverse dipolar impedances in the low-frequency limit have the form [33,34]: $Z_{\parallel} = -i\omega Z_0/(2\pi c) \int_0^L ds (d')^2$ and $Z_{\perp} = -i(Z_0/\pi) \int_0^L ds (d'/d)^2$, where $d(s)$ is the local radius of the beam pipe, $d'(s)$ is the slope of the taper and L is the total length of the taper. Examples of the first type are the transitions between the $r = 23.5$ mm arc and $r = 14$ mm straight-section chambers. The AR design generally abides by the 10:1 tapering rule, in this case $L = 94$ mm.

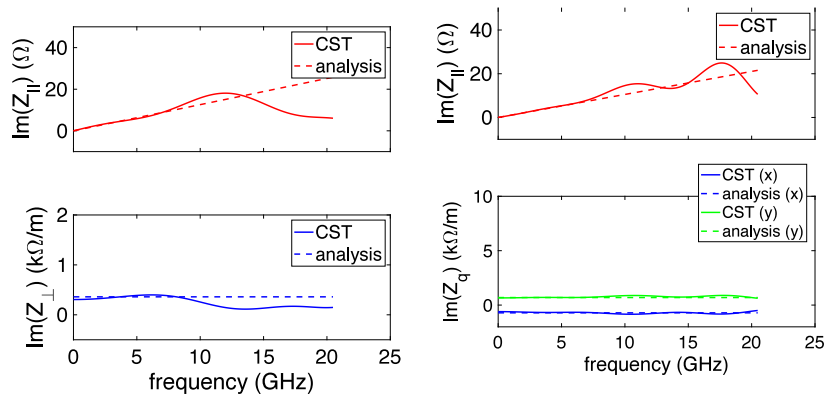


Fig. 6. Impedance of tapered transitions: Comparison between the CST simulations and theory, left: imaginary part of impedance for the round transition model (longitudinal and transverse), right: imaginary part of impedance for the impedance of elliptical transition model (longitudinal and transverse quadrupolar impedance).

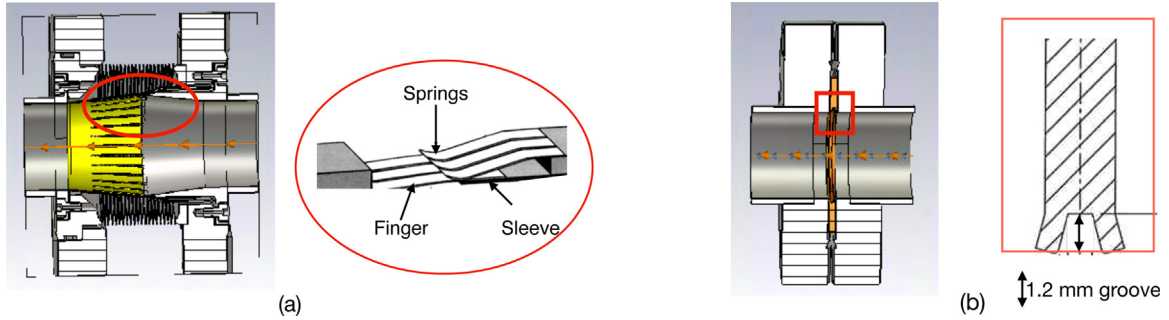


Fig. 7. Left (a): Bellows with rf shielding. Right (b): AR adopted flange and gasket design.

The transitions of the second type are those between the $r = 14$ mm round arc and the elliptical dipole chamber ($a = 20$ mm and $b = 7$ mm semi-axes), with a transition length $L = 43.6$ mm (shorter than the values given by the 10:1 tapering rule, due to limited chamber space). They are the most prevalent (three pairs per sector) and represent a relatively large contribution to the overall transverse impedance budget in the AR (as shown in Table 1). The larger impedance is in the vertical plane, and can be estimated as $Z_y \approx -i(2Z_0/\pi)(r_1 - b)^2/(Lbr_1)$ [33]. These transitions are also the main source of the quadrupolar wakefields [34]. Fig. 6 compares the CST numerical calculation (solid) and theory (dashed) for both transition types, showing good agreement in the frequency range below the chambers' cut-off.

Bellows with RF shielding. A large number of chamber sections connect through bellows to absorb chamber-to-chamber misalignment and thermal expansion during vacuum baking. Good shielding from rf fingers is essential to restore electric continuity and avoid electromagnetic field trapping [35]. The below model with rf fingers is shown in the left images of Fig. 7. The fingers, relatively few and wide, are similar to the National Synchrotron Light Source (NSLS)-II design [36]. Simulations indicate critical sensitivity to good sealing of the rf fingers, which should be of concern during installation.

Flanges and Gaskets. Several variants of flange designs [37,38] have been studied in both rings including one using an ATLAS-type gasket [39]. The depth of the gasket groove is a sensitive impedance parameter, due to the large number of flanges. Our previous flange design with larger grooves in the AR gasket led to a charge per bunch threshold for the longitudinal single bunch instability that was 3 times smaller than what we have presented here. We found that bellows with poor RF shielding or a larger groove depth in the gasket have the potential to affect single-particle dynamics and decrease the injection efficiency [15]. The current gasket design has a groove with depth ≈ 1.2 mm (right image in Fig. 7), which satisfies mechanical constraints and is still acceptable from the impedance standpoint.

3.4. Key parameters for the impedance budget

Following common practice, we categorize the impedance contributed by distinct sources in terms of a few key parameters as a way to provide a rough ranking in terms of contributions to the total impedance budget, and potentially identify problems with the vacuum design. While this is no substitute for beam-dynamics studies based on the full spectral content of the impedance, this is often a first useful step towards a full characterization of impedance effects. These metrics include the loss factor, kick factor, and the RL-fitting parameters. These are briefly described below.

3.4.1. Loss factor and RL fitting for longitudinal wakefield

The loss factor κ_z (units of V/C) can be expressed in terms of longitudinal impedance or wake function:

$$\kappa_z = \frac{1}{2\pi} \int_{-\infty}^{\infty} Z_z(\omega) \tilde{\lambda}^2(\omega) d\omega = \int_{-\infty}^{\infty} W_z(z) \lambda(z) dz, \quad (3)$$

where $\lambda(z)$ is the longitudinal bunch profile and $\tilde{\lambda}(\omega)$ its Fourier transform. In our evaluation of loss factor we use a Gaussian profile for the electron beam.

In addition, following [5,19,40], effective resistive R and inductive L components have been determined by fitting the wake potential to the $R+L$ model, where the wakefield curve is fit to the sum of a purely resistive wake, proportional to the longitudinal charge distribution $\lambda(s)$, plus a purely inductive wake proportional to the derivative of the current, $\lambda'(s)$:

$$W_{R+L}(z) = -Rc\lambda(z) - c^2L\lambda'(z). \quad (4)$$

We find the fit $R = 468 \Omega$, $L = 18$ nH for the total AR wakefield as in Fig. 8, which shows the comparison between the real short range wakefield and the fit. As a rough way to characterize the rings, we say the AR is more inductive with the ratio of $R\sigma_z/(cL) < 1$ ($\sigma_z = 5$ mm), the wakefield looks more like the derivative of the bunch shape, and

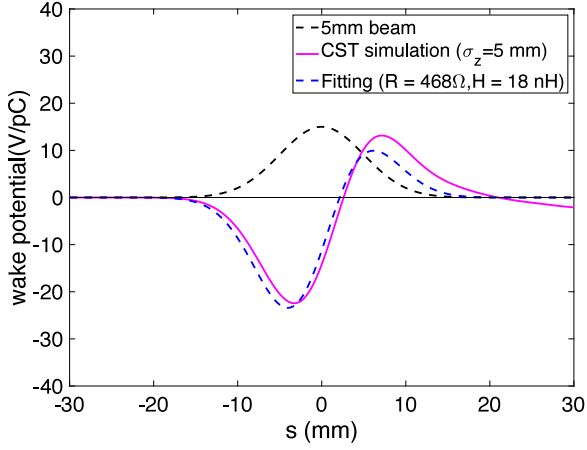


Fig. 8. Comparison between the total longitudinal wake field in the AR for 5 mm Gaussian beam from CST with the fitted R+L model.

the front of a nominal bunch loses energy while the tail gets much of that energy back.

We define a goodness-of-fit parameter by:

$$g_{\text{fit}} = 1 - \frac{\sqrt{\int (W(s) - W_{R+L}(s))^2 \lambda(s) ds}}{\sqrt{\int W(s)^2 \lambda(s) ds}} \quad (5)$$

The AR model fits well with $g_{\text{fit}} = 0.84$.

The corresponding parameters in the SR are as $R = 613 \Omega$ and $L = 27 \text{ nH}$, which characterize the SR as a more resistive ring, with the ratio of $R\sigma_z/(cL) > 1$ ($\sigma_z = 14 \text{ mm}$), so the total wakes look like the mirror image of the bunch shape, and the whole bunch loses energy due to short-range wakefields.

The resistive and inductive components can then be used to define the real and imaginary part of a normalized impedance according to

$$\frac{Z_z}{n} = \frac{\omega_0 \sigma_z}{c} R + i\omega_0 L, \quad (6)$$

with Z_z the impedance at a representative frequency ω , and $n = \omega/\omega_0$ where the revolution frequency $\omega_0 = 2\pi c/C$, with C the ring circumference. Thus, we have $|Z/n| = 0.21 \Omega$ for the AR impedance model, and $|Z/n| = 0.43 \Omega$ for the SR model.

3.4.2. Boussard criterion with longitudinal impedance budget

The Boussard criterion is often used as a first estimation of the instability threshold [41,42]. It is known to give a rough and conservative estimate of the threshold to a strong instability. According to this criterion, the threshold bunch charge is given by:

$$Q_{th,B} = (2\pi)^{3/2} \frac{\alpha \sigma_z E \sigma_\delta^2}{c |Z/n|} \quad (7)$$

with α the momentum compaction factor, E the beam energy, σ_δ the relative beam energy spread, and $|Z/n|$ the effective impedance.

For the accumulator ring, taking $\alpha = 1.1 \times 10^{-3}$, $E = 2 \text{ GeV}$, $\sigma_\delta = 0.84 \times 10^{-3}$, and $|Z/n| = 0.21 \Omega$, we obtain $Q_{th,B} = 1.91 \text{ nC}$, which is about 66% higher than the design working point with 1.15 nC per bunch. In other words, the threshold of the effective impedance is $|Z/n|_{th,B} = 0.34 \Omega$ for the design charge of 1.15 nC per bunch.

For the storage ring, where we have $\alpha = 2.025 \times 10^{-4}$, $E = 2 \text{ GeV}$, $\sigma_\delta = 1.02 \times 10^{-3}$, and $|Z/n| = 0.43 \Omega$, we obtain $Q_{th,B} = 0.77 \text{ nC}$, which is 33% lower than the design charge of 1.15 nC per bunch.

The Boussard criterion is generally over-conservative and will tend to predict a lower threshold than simulations [43]. The simulation results for AR and SR based on beam-dynamics study with pseudo-Green functions are presented in Sections 4 and 5 respectively. Our experience indicates that the accuracy of the Boussard criterion depends on the

character of the total wakefield. If the ring is more inductive, as is the case for the AR, the Boussard criterion can be quite conservative, and is about 8 times more stringent than indicated by the simulations. While for the SR, where the total wakefield is more resistive, the Boussard criterion is closer to the simulations, but still about 3 times more restrictive.

3.4.3. Kick factor and tune shift for transverse wakefield

One of the main parameters that impacts transverse beam dynamics is the beta-function-weighted transverse impedance:

$$\beta Z_x(z) = \sum_{j\text{-source}} \beta_{x,j} Z_{x,j}(z), \quad (8)$$

$$\beta Z_y(z) = \sum_{j\text{-source}} \beta_{y,j} Z_{y,j}(z). \quad (9)$$

where $\beta_{x,j}$ and $\beta_{y,j}$ are respectively the horizontal and vertical beta function at the j th impedance source.

The kick factor $\kappa_{\perp,j}$ (units of V/C/m) contributed by the j th impedance source is:

$$\kappa_{\perp,j} = \frac{1}{2\pi} \int_{-\infty}^{\infty} \tilde{\lambda}(\omega) Z_{\perp,j}(\omega) d\omega = \int_{-\infty}^{\infty} \lambda(s) W_{\perp,j}(z) dz, \quad (10)$$

which is associated with the coherent tune shift:

$$\Delta v_{\perp,j} = -\frac{Q_b \beta_{\perp,j} \kappa_{\perp,j}}{4\pi E/e}, \quad (11)$$

where Q_b is the bunch charge. The total kick factor κ_{\perp} and coherent tuneshift Δv_{\perp} result from the sum over all the impedance sources. The effective transverse impedance is also introduced as

$$Z_{\perp}^{\text{eff}} = 2\sqrt{\pi} \sigma_r \kappa_{\perp}. \quad (12)$$

3.5. Macroparticle simulation studies

One general method to simulate beam dynamics affected by wakefields is to apply the macro-particle simulation code ‘*elegant*’ [20], which offers the *ILMATRIX* element, which is an individualized linear matrix for each particle for fast symplectic tracking through all or a portion of the ring, including chromatic and amplitude-dependent effects. The wakefield is applied using the *WAKE* and *TRWAKE* elements, which use the longitudinal and transverse pseudo-Green functions respectively to represent the whole impedance budget. The *elegant* code, by doing the convolution between the density distribution and the pseudo-Green functions, applies the wakefield kick (both longitudinal and transverse) to the beam in a manner which is updated for each pass based on the distribution at that moment, and tracks the particles while approaching the equilibrium state. A consistency check for the longitudinal pseudo-Green function is presented in Section 7.3.

Longitudinal. *Elegant* was applied to study the longitudinal microwave instability (MWI) [44]. Tracking was done with the 1 mm drive-beam wake potential calculated with CST and analytical formulas (RW) to represent the wake function, with the appropriate flag in the *elegant* “WAKE” command set to accept violation of causality. The charge per bunch was gradually increased for each run, and we monitored the evolution of the bunch to check the bunch lengthening effect due to short-range wakefields [4,45], as well as the energy spread growth due to MWI. The MWI threshold is determined by noting that the equilibrium energy spread remains constant below the MWI threshold, and only starts to increase above the MWI threshold [44,46].

Transverse. The transverse mode coupling instability (TMCI) [47–49] was studied by launching the beam with an initial small transverse offset and monitoring the evolution of the beam centroid. The threshold of TMCI was determined by gradually increasing the charge per bunch for each run, and monitoring the evolution of the beam centroid until instability and exponential growth was observed.

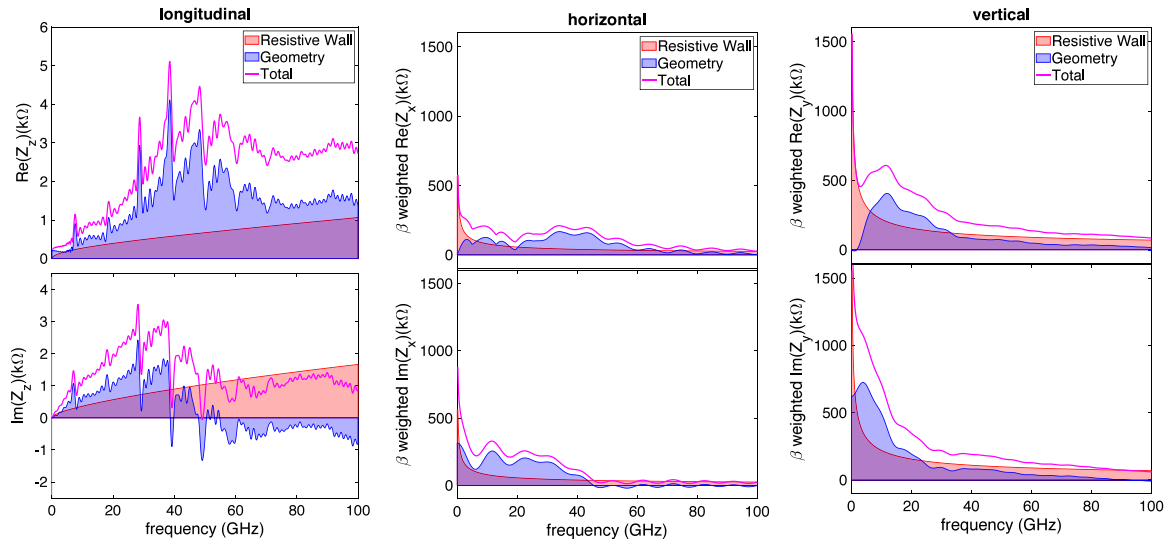


Fig. 9. For the AR, impedance budget from a 1 mm drive beam in CST, from each component and the total. Upper: Real component of the impedance Z . Lower: Imaginary component of the impedance. Shown from left to right are the longitudinal impedance (a) and (b), beta-weighted horizontal impedance (c) and (d), and beta-weighted vertical impedance (e) and (f).

Table 1

For the AR, associated key parameters of broadband impedance (longitudinal and transverse) for the relevant sources. Calculation of factors for an rms bunch length of 5 mm. Components are ordered by tune shift in the vertical plane (last column).

Component	No.	Single component					Total				
		κ_z V/pC	$\text{Re}(Z_z/n)$ m Ω	$\text{Im}(Z_z/n)$ m Ω	κ_x V/pC/m	κ_y V/pC/m	κ_z V/pC	$\text{Re}(Z_z/n)$ m Ω	$\text{Im}(Z_z/n)$ m Ω	Δv_x (10^{-4})	Δv_y (10^{-4})
Resistive wall	1	3.090	31.40	61.70	509.2	651.4	3.090	31.40	61.70	-1.553	-3.465
Arc transition	36	0.004	0.018	0.871	0.230	0.230	0.144	0.659	31.37	-0.068	-2.699
Flange	240	0.001	0.009	0.219	2.300	2.300	0.209	2.088	52.49	-1.066	-1.156
Straight transition	12	0.041	0.413	2.109	5.500	5.500	0.492	4.958	25.31	-0.453	-0.177
Pump screen	48	0.001	0.006	0.098	0.580	0.580	0.028	0.278	4.680	-0.010	-0.133
Bellows	84	0.014	0.144	0.241	0.850	0.850	1.193	12.12	20.24	-0.297	-0.128
BPM	72	0.001	0.014	0.040	2.600	2.600	0.101	1.022	2.873	-0.053	-0.084
Inline pump	48	0.000	0.001	0.032	0.850	0.850	0.144	0.059	1.546	-0.103	-0.043
RF Cavity	2	0.980	9.930	-7.097	7.800	7.800	1.960	19.86	-14.19	-0.107	-0.036
Longitudinal feedback	1	0.490	4.969	-3.383	5.100	5.100	0.490	4.969	-3.383	-0.035	-0.012
Cavity transition	2	0.088	0.898	1.973	1.200	1.200	0.176	1.796	3.946	-0.036	-0.012
LFB transition	1	0.075	0.765	1.620	0.032	1.100	0.075	0.765	1.620	-0.016	-0.005
Stripline kicker	1	0.010	0.087	0.000	0.530	0.510	0.010	0.087	0.000	-0.004	-0.001
Ring total							8.112	80.06	188.2	-3.801	-7.950

4. AR results

All the AR vacuum chambers are circular, with the exception of the elliptical vacuum chambers in the dipole magnets. The RW impedances of chambers with elliptical cross-section can be obtained from the formulas for a round chamber with radius matching the smaller semi-axis, using the Yokoya factors given above. Finite-resistivity elliptical chambers also generate quadrupole wakes, but for the AR these are a minor effect and will be ignored in this analysis of the beam dynamics. The dipole vacuum chamber sections also differ in that they are NEG coated for better vacuum quality. For these, Eqs. (1) and (2) are used, corrected with the appropriate Yokoya factors.

Impedance budget. The CST calculation for the total impedance and breakdown into the main components is shown in Fig. 9.

Budget table. The associated key parameters of broadband impedance (longitudinal and transverse) for the relevant sources in the AR are shown in Table 1, which includes the longitudinal loss factor, normalized impedance (both real part and imaginary part), the transverse kick factors and corresponding tune shift from components, following the definitions in Section 3.4. The parameters are calculated for an rms bunch length of 5 mm.

Beam dynamics study. The macro particle simulation code *legant* [20] was applied to study the longitudinal and transverse single-bunch instabilities. The simulation results (Fig. 10) show a longitudinal MWI instability threshold at about 15 nC/bunch. Calculations for the instability threshold by analysis of the corresponding Vlasov-Fokker-Planck equation [50] gave very similar results.

The TMCI was studied by launching the beam with an initial small transverse offset (0.1 mm) and monitoring the evolution of the beam centroid. A threshold is observed at $Q \sim 5.8$ nC per bunch, as shown in Fig. 11 for the vertical plane (in the horizontal plane the threshold is somewhat higher).

In conclusion, the instability thresholds in both the transverse and longitudinal planes appear to be safely above the AR design charge of 1.15 nC per bunch.

5. SR results

An accurate model of the resistive-wall impedance was constructed based on a detailed segmentation of the vacuum chamber for arcs and straight sections. For the vacuum chamber in the SR we use the segmentation concept involving three materials (Cu, Al, and stainless steel, with conductivity $\sigma_c = 5.8 \times 10^7$, 1.7×10^7 , and 1.3×10^6 $\text{m}^{-1}\Omega^{-1}$, respectively), and NEG coating with $\sigma_c = 0.66 \times 10^7$ $\text{m}^{-1}\Omega^{-1}$.

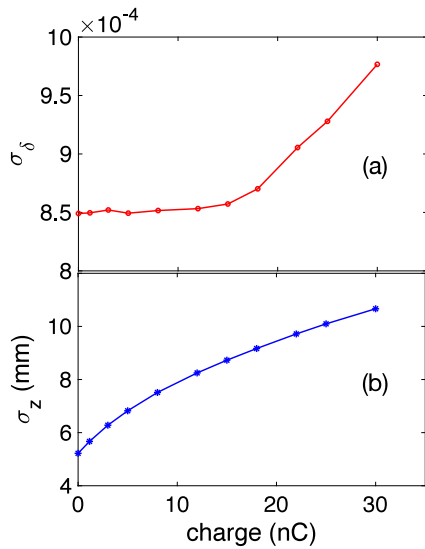


Fig. 10. AR: Single-bunch longitudinal dynamics simulations indicate a ~ 15 nC/bunch threshold for the onset of a microwave instability. The two images show the rms bunch length (upper) and relative energy spread (lower) vs. bunch charge after about 2.5 damping times.

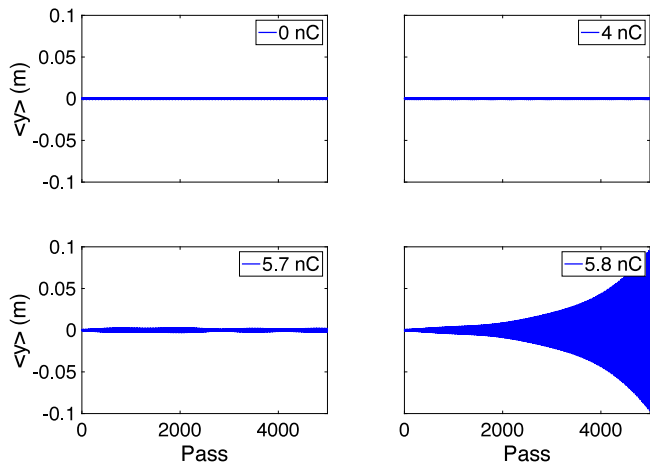


Fig. 11. AR: TMCI simulations place the instability threshold just below $Q_b = 5.8$ nC.

Impedance budget. The CST calculation for the total longitudinal and transverse impedance, as well the breakdown in the main components is shown in Fig. 12.

Budget table. The associated key parameters of broadband impedance (longitudinal and transverse) for the relevant sources in the SR is shown in Table 2, which follows the same format as for the AR, while the parameters are calculated for the nominal rms bunch length of 14 mm.

Beam dynamics study. Two distinct modes are modeled in the simulations of the SR single bunch instability: one is the design operation mode, where the high order harmonic cavities (HHC) are used to yield a flat-top bunch profile with a factor of about 4 bunch lengthening, and the equilibrium bunch is a flat-top beam with nominal bunch length about 14 mm rms. The other mode is to turn off the HHC in simulations to mimic the commissioning stage of the machine, when beam current is too low to drive the HHC and the equilibrium bunch is a Gaussian beam with nominal bunch length about 3.5 mm rms. In both modes, the design charge per bunch is 1.15 nC from the AR injection, but the latter mode has fewer bunches thus lower average current.

The macro-particle simulation code *elegant* [20] was applied to study the longitudinal and transverse single-bunch instabilities. The

simulation results (Figs. 13 and 14) show an instability threshold at about 4 nC/bunch with HHC and 2 nC/bunch without HHC.

Fig. 15 summarizes the macro-particle-simulation study for three impedance models including (i) resistive wall impedance only, (ii) geometric impedance only and (iii) the combination of the two. We determined the instability threshold in the presence and absence of harmonic cavities. For the transverse head-tail instability study we also vary the chromaticity of the machine, which can go up to 4 to 5 without diminishing the beam lifetime [51,52]. At vanishing chromaticities, the simulation results indicate an instability threshold below the design bunch charge where the presence of harmonic cavities is shown to aggravate the instability [53]. Positive chromaticities have the expected stabilizing effect, particularly when the bunch is lengthened by the harmonic cavities. Chromaticities of $\xi_y \sim 0.2$ and $\xi_x \sim 1.4$ are seen to stabilize bunches with the nominal charge of 1.15 nC with and without harmonic cavities respectively.

With the harmonic cavities off, the observed irregular behavior of the curves is a result of various head-tail modes coming in and out of play in driving the instability. The simulation does not yet include a model of the transverse feedback system, which in the ALS is found to be quite effective at raising the transverse instability threshold [54].

6. Benefits of impedance workflow on ring design

By generating an approximate but rapid estimate of the threshold for various instabilities, this workflow allows for repeated cycles of identifying beamline elements which could be an issue, generating improved designs, and assessing the impact of the updated designs. This process also allows for quick responses to questions about the ring design or the simulation methods. Two examples are described below for how vacuum element designs which impacted the total impedance budget were optimized through this feedback process. The flange design, described earlier, was also improved.

Pump slots. The two designs of the pump screen are shown in Fig. 16(a) and (b), being the original and revised designs respectively. The key parameters of the pumping slots are the slot length l and slot width w , which determine the impedance at low frequencies as $Z_{\parallel} \propto (\omega^3(0.1814 - 0.0344\omega/l))$ [27,55].

Generally speaking, the narrower slots lead to lower impedance. We have modified the original model (a), having one wide slot with $w = 12$ mm to the model (b), having 3 slots each with $w = 4$ mm to keep the same vacuum conductance while reducing the longitudinal wakefield as shown in Fig. 16(c).

Collimator with transitions. We had two collimators for beam scraping in the storage ring, and together they are the second largest source for the vertical tune shift as shown in Table 2. The model used is borrowed from the current ALS design as shown in Fig. 17(a); the blue part is the vacuum part and the surrounding materials are perfect electrical conductor (PEC). The gap between the metal scrapers (gray parts shown in the figures) is about 2.8 mm. We revised it as shown in Fig. 17(b), where we added a tapered transition to avoid a sudden change in the chamber profile. We are using a 5 mm (the natural bunch length in the AR) drive beam in CST. The revised collimator has reduced the vertical wakefield almost in half as shown in Fig. 17(c).

Photon absorbers. Photon absorbers are distributed around the SR to limit and control photon heating and, while this is a common component of storage rings, there is little literature available considering the impact on impedance. We found that the impedance is strongly impacted by the crotch absorbers inserted into the beam pipe because there is strong coupling from the beam to the absorber cavities from the beam pipe opening, and also because there are more than 20 absorbers in the entire ring. Thus, the resonant impedance can cause transverse instability. Mitigation of the absorber impedance was challenging because it has to be coordinated with studies of the photon scattering and

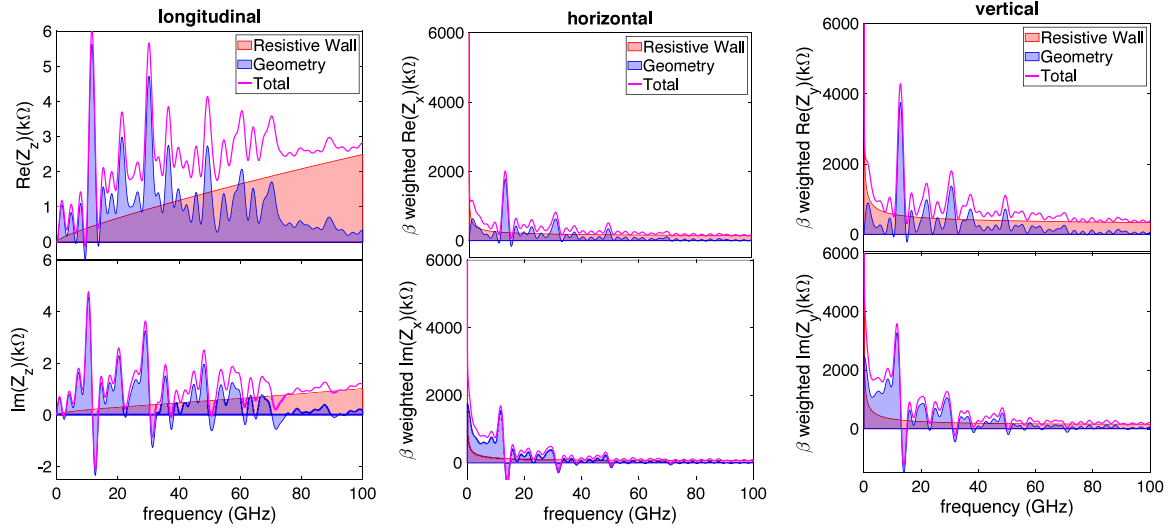


Fig. 12. For the SR, impedance budget from a 1 mm drive beam in CST, from each component and the total. Upper: Real component of the impedance Z . Lower: Imaginary component of the impedance. Shown from left to right are the longitudinal impedance (a) and (b), beta-weighted horizontal impedance (c) and (d), and beta-weighted vertical impedance (e) and (f). Note that the artificial negative value in $\text{Re } Z$ is due to the limited simulation range of the trapped modes, which does not affect the broad-band impedance calculation.

Table 2

For the SR, associated key parameters of broadband impedance (longitudinal and transverse) for the relevant sources. Calculation of factors for an rms bunch length of 14 mm. Components are ordered by tune shift in the vertical plane (last column).

Component	Quantity	Single					Sum				
		κ_z V/pC	$\text{Re}(Z_z/n)$ m Ω	$\text{Im}(Z_z/n)$ m Ω	κ_x V/pC/m	κ_y V/pC/m	κ_z V/pC	$\text{Re}(Z_z/n)$ m Ω	$\text{Im}(Z_z/n)$ m Ω	Δv_x $\times 10^{-4}$	Δv_y $\times 10^{-4}$
RW	1	-0.481	38.304	90.037	1063.570	2090.861	-0.481	38.304	90.037	1.703	3.827
Collimator	2	-0.000	-0.121	19.680	426.245	426.245	-0.000	-0.243	39.360	0.683	1.560
Flange	384	-0.000	-0.012	0.198	1.243	1.243	-0.002	-4.542	76.103	0.486	0.988
Transitions ^a	10	-0.045	3.566	3.422	9.030	47.985	-0.448	35.660	34.218	0.145	0.878
Gate valve	48	-0.000	0.009	0.519	3.869	3.869	-0.000	0.449	24.900	0.334	0.704
BPM ^{a,b}	216	0.000	-0.017	0.092	0.622	0.622	0.046	-3.689	19.841	0.072	0.270
Arc-keyhole	12	-0.038	2.572	5.987	44.373	6.299	-0.459	30.868	71.840	0.731	0.173
HHC	1	-0.511	40.683	-21.783	5.812	5.812	-0.511	40.683	-21.783	0.028	0.032
Absorber	50	-0.008	0.617	1.437	38.918	0.441	-0.388	30.868	71.840	0.890	0.017
LFB	1	-0.262	20.861	-15.069	5.946	5.946	-0.262	20.861	-15.069	0.010	0.011
RF cavity	2	-0.600	47.788	-31.877	0.000	0.000	-1.200	95.575	-63.754	0.000	0.000
Ring total							-3.703	284.795	327.533	5.081	8.460

^a(including some bellows).

^b(including some bellows).

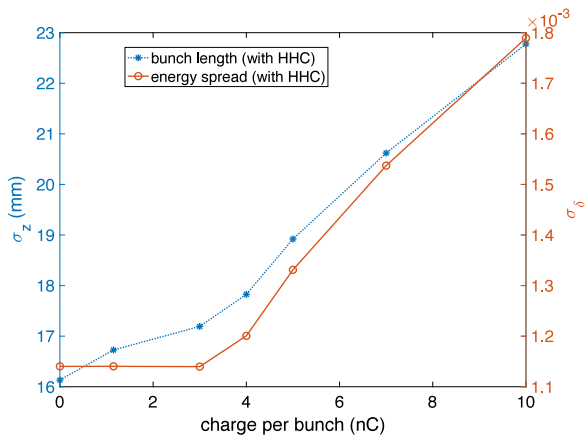


Fig. 13. SR: With HHC, single-bunch longitudinal dynamics simulations indicate ~ 4 nC/bunch threshold for the onset of the instability. The rms bunch length (left) and energy spread (right) are reported vs. bunch charge after about 2.5 damping times.

thermal dynamics. We finally reach a design that gradually transitions to a narrower beam pipe opening as shown in Fig. 18(b), compared to the original design without impedance considerations (Fig. 18(a)), and we also modified the absorber to follow the beam pipe opening to reduce the coupling between the beam and the absorber chamber. The modified model has a much small dipolar impedance as shown by comparing Fig. 18(c) and Fig. 18(d).

7. Additional consistency checks

As discussed in Section 3.3, we cross-check the CST calculations with analytical formulas as much as applicable [27]. Fig. 6 is an example of the comparison between simulations and formulas, which also demonstrates one way to cross-check our calculations. Good agreement at low frequencies indicates that we have the correct settings in CST simulations.

We cross-checked our impedance modeling in multiple ways, which justified our view of the accuracy of the calculations. More examples and discussions of these consistency checks are presented in the following sections.

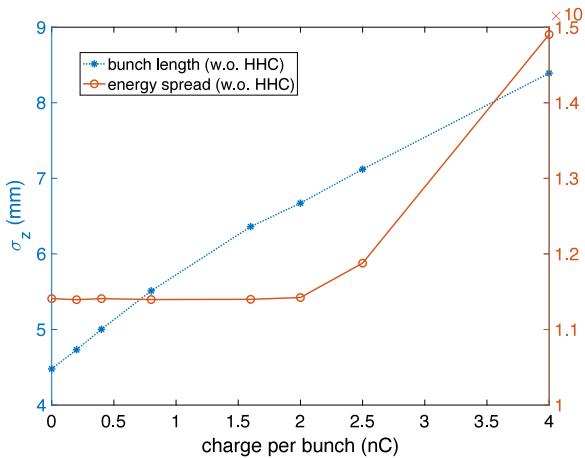


Fig. 14. SR: Without HHC, the single-bunch longitudinal instability threshold is at about 2 nC/bunch. The rms bunch length (left) and energy spread (right) are reported vs. bunch charge after about 2.5 damping times.

7.1. RF cavity impedance

Properties of individual modes in the rf cavities below the rf frequency cutoff can be examined using the simulation code T3P [56]. The numerical contribution of those modes to the longitudinal loss factor of the AR rf cavity is given by

$$\kappa_l \simeq \sum_n \frac{\omega_n}{4} \left(\frac{R}{Q} \right)_n \tilde{\lambda}(\omega_n, \sigma_z) \simeq 0.63 \text{ V/pC}$$

where $(R/Q)_n$ is the mode amplitude, $\tilde{\lambda}(\omega_n, \sigma_z)$ the bunch form factor at the mode frequency, and the sum only includes modes below the cutoff frequency, such that $\omega_n/2\pi < f_c \simeq 2.4c/2\pi b \approx 3.1$ GHz. This leaves out the modes above cutoff, but their contribution can be approximated using the diffraction model [30]:

$$\kappa_d \simeq \frac{Z_0 c}{4\pi^2 b^2} \sqrt{g/\sigma_z} \left[\Gamma(1/4) - 4\sqrt{\omega_c \sigma_z/c} \right] \simeq 0.40 \text{ V/pC.}$$

The sum of these two terms, $\kappa_l + \kappa_d = 1.03$ V/pC agrees well with the direct calculation of 0.98 V/pC using CST.

7.2. Separation of resistive wall impedance and geometric impedance

Our work follows the general method of separating the short-range wakes into purely geometrical terms, which neglect the resistivity of the walls, and resistive wakes which are calculated for mode properties that are approximated as only weakly affected by the resistivity. We justified the separation in multiple ways. Firstly, for the smooth components with a fixed cross-section, resistive wall impedance from CST simulations agree well with analytical formulas in the form of the Yokoya factor, as shown in Fig. 19, where we have an aluminum elliptical chamber with a length of 0.3 m and a vertical semi-axis of 5 mm in the simulation. When using perfect conducting boundary conditions instead of aluminum material in CST, the results are at noise level for the impedance which agrees with the physics.

Secondly, for the specialized components listed in the budget tables, the geometric impedance is far larger than the resistive wall impedance. Thus, rough approximations of the resistive wall effect for these elements should not have much impact. One example is the arc-keyhole chamber, where the round beam pipe has an opening on the horizontal plane to let the radiation out. The keyhole chamber has a relatively large resistive wall impedance due to the small radius (10 mm) and the relatively long chamber length (1.5 m). Still, for a single keyhole chamber, the resistive wall horizontal kick factor is 0.0032 V/pC/m, which is orders of magnitude smaller than for the geometric impedance where the horizontal kick factor is 44.373 V/pC/m as listed in Table 2.

7.3. Pseudo-Green functions

To study the beam dynamics, a driving beam with 1/5 of the nominal bunch length, or even shorter, is chosen to obtain the pseudo-Green function in both rings through numerical simulations using CST, which is then applied within a beam dynamics code such as *elegant*.

Fig. 20(a) shows the pseudo-Green function in the AR, which is the total wake potential curve of a 1 mm drive beam (magenta curve). We have cross-checked the pseudo-Green function, by doing the convolution of the 1 mm beam's wake potential (magenta curve in Fig. 20(a)) with a 5 mm Gaussian distribution to get the blue curve in Fig. 20(b), and then compared it with the direct result of a 5 mm drive beam in CST simulations (magenta curve in Fig. 20(b)).

The comparison shown in Fig. 20(b) indicates acceptable overall agreement. The discrepancy of the two curves can be attributed to a comparatively long bunch used for the pseudo-Green function calculation.

7.4. Non-Gaussian beam in the SR

The beam in the CST wakefield solver is a Gaussian beam with a self-defined bunch length. The real beam in the storage ring with HHC is a stretched flat-top beam (rms 14 mm) or a double-horn distribution when overstretched, which is done to further increase the beam lifetime [57]. The impedance budget table for the SR shows the key impedance parameters of a Gaussian beam with rms bunch length of 14 mm. This allows for a quick comparison of impedance contributions from each component, while the beam dynamics study in the *elegant* code is based on a convolution of the pseudo-Green functions, automatically recalculating the wakefields for a given distribution.

We compared the frequency spectrum of the 14 mm Gaussian beam with the more realist flat-top beam and double-horn beam as shown in Fig. 21, which indicated that a 14 mm Gaussian beam covers the main frequencies we are concerned about for both realistic distributions.

7.5. Impedance budget with weldment errors

No weldment or flange joint can be made perfectly, and offsets between components inside the wall will cause step transitions distributed along the ring which will change the total impedance budget. As many of these joints are distributed along the ring, this can be a potential source of discrepancy with impedance modeling. We have analyzed different models of weldment error and step transitions and, finally, choose a step of 0.5 mm error as a conservative estimate for the typical weldment error. We add over 500 of these errors into the impedance budget, as every two-component and two-chamber joint contributes one error. The pseudo-Green functions with (red) and without (blue) weldment errors are shown in Fig. 22(a).

We update the beam dynamics study with the pseudo-Green functions that include weldment errors, and while we observe no change to the instability threshold, the errors do affect the details of the beam dynamics. An example of this is shown in Fig. 22(b) for the microwave instability study with a 4 nC bunch without HHC; the case where weldment errors are included shows some instability suppression due to the inductance of the impedance errors from the step transitions. This is similar to previous work on impedance modeling which indicates that inductive impedance helps to suppress some of the instabilities in the ring [5].

This change in the impedance budget and dynamics due to weldment errors around the ring, which has not been reported previously in the literature, indicates a possible source for the common problem of inconsistencies between impedance modeling and beam-based measurement [7]. There is significant ongoing research into resolving these inconsistencies and to improve the impedance modeling for a more accurate prediction on beam dynamics, however, the goal is challenging as the beam dynamics is complicated by collective effects [4,42,58].

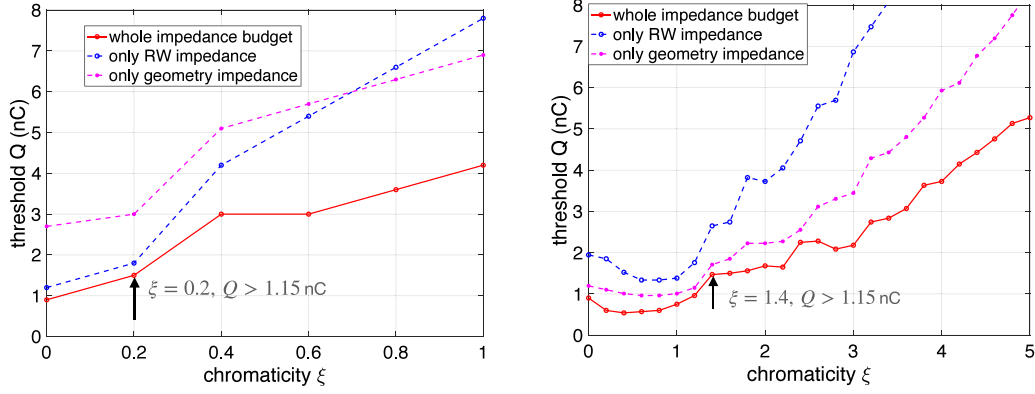


Fig. 15. SR: Single-bunch vertical instability threshold as a function of the vertical chromaticity including resistive-wall impedance only (blue line), geometric impedance only (magenta curve) and total impedance (red curve). Results are with (left) and without (right) HHC. For vanishing chromaticity the threshold is lower than the design bunch charge but it improves quickly with finite chromaticity. Chromaticities of $\xi_y \sim 0.2$ and $\xi_y \sim 1.4$ are seen to stabilize 1.15 nC nominal-charge bunches with and without harmonic cavities respectively.

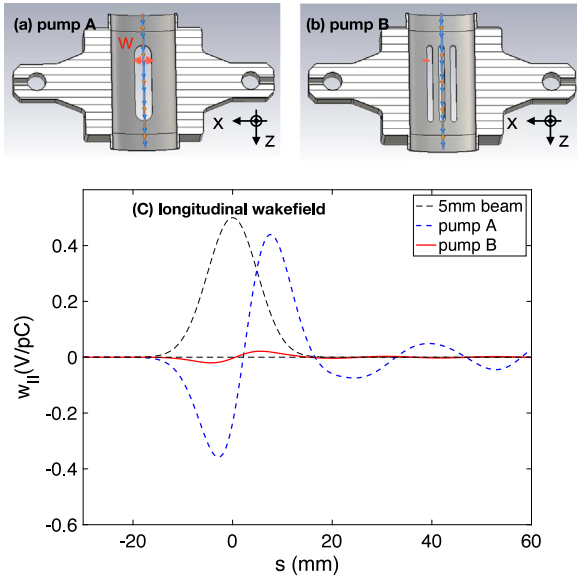


Fig. 16. Two designs of the pump screen: (a) the original simplified one and (b) the revised one to reduce the wakefield and keep the same vacuum conductance; (c) comparison of the longitudinal wakefield of two models.

Our study shows that weldment errors and other variations from the idealized vacuum design may alter the dynamics in the ring but also suggests that, for the ALS-U, it is unlikely for these types of errors to dramatically alter more critical behaviors such as the threshold current for the onset of instabilities. The work presented here will serve as a record for cross-checking with future measurements in the upcoming ALS-U.

8. Conclusions

In summary, we have presented a systematic calculation of the impedance for the upcoming ALS-U, together with optimizations, consistency checks, error analysis, and its application to the analysis of collective effects. In the study, we have described the general workflow to build the impedance budget in the accelerator rings, and presented systematic results for the ALS-U project for both the 3rd generation light source type ring of the accumulator ring (AR) and the 4th generation light source MBA ring of the storage ring (SR). The key parameters for impedance are introduced and the RL fitting model and Boussard

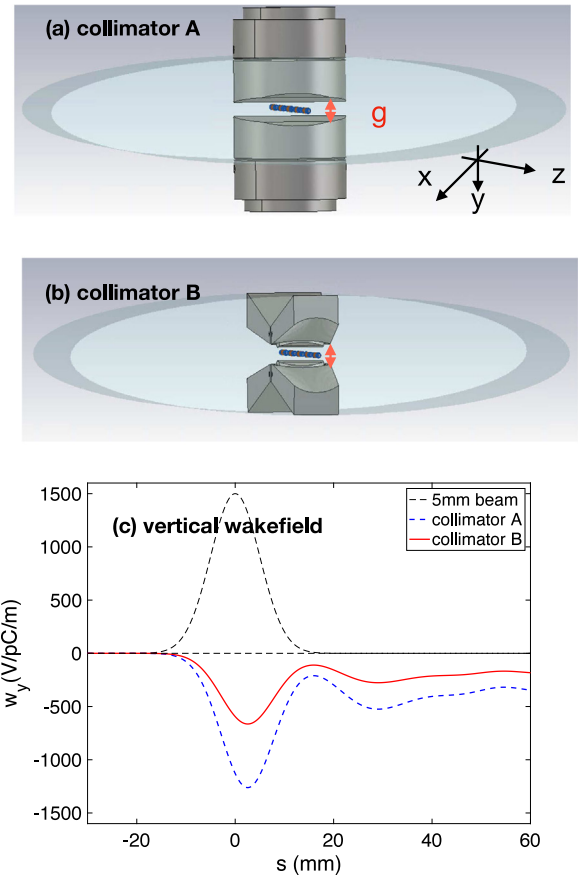


Fig. 17. Two simplified models of the collimators in CST: (a) the current one and (b) the revised one under consideration to reduce the wakefield; (c) comparison of the vertical wakefield of the two models.

criterion are discussed. We also present alternative ways to cross-check the simulation results for reliable impedance models, such as comparison between CST simulations and analytical formulas at low frequency, consistency checks for the separation of impedance sources into resistive wall and geometric contributions, accuracy estimates for the pseudo-Green functions, and evaluating the impact of weldment errors on the impedance budget. Modeling of the ALS-U impedance and beam dynamics studies suggest a large safety margin for both longitudinal and transverse single-bunch instability thresholds in the AR.

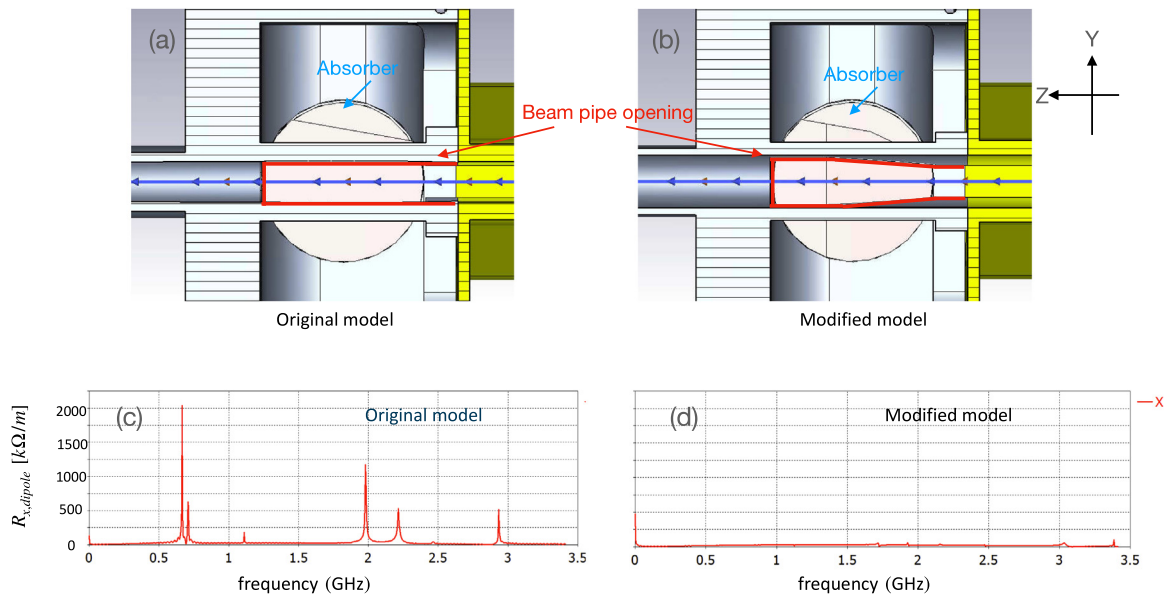


Fig. 18. Impedance mitigation of photon absorber in the storage ring: (a) original model of the absorber chamber with beam pipe; (b) modified model with transitioned beam pipe opening; (c) horizontal dipolar impedance of original model; (d) horizontal dipolar impedance of modified model, which has much smaller impedance compared to results shown in (c).

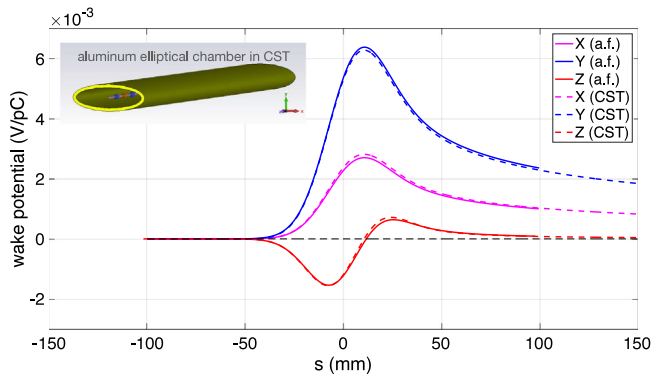


Fig. 19. Comparison of the wakefield from analytical formulas (a.f.) for resistive wall impedance with CST results on a smooth aluminum elliptical chamber.

The margin in the SR is about 2-fold of the design charge (longitudinal instability, with high-order harmonic cavity), which is smaller than the AR due to the narrower beam pipe and complicated insertion devices in the storage ring.

The workflow presented here has identified key elements that were consuming too much of the overall impedance budget, and allowed for repeated optimizations of those elements, especially the pump screen, collimator blades and photon absorbers.

This paper presents the application of impedance modeling methods to the study of a new-class light-source machine characterized by unusually narrow vacuum-chamber apertures, following best practices in the field and extending them to include effects which have not been previously considered. The results of this analysis give strong reassurance that impedance effects will be manageable and will not compromise the intended performance of the machine. This outcome is a critical result for the ALS-U project and was not a foregone conclusion, considering the impedance-effect challenges posed by the new generation of machines.

CRediT authorship contribution statement

Dan Wang: Conceptualization, Methodology, Data curation, Formal analysis, Writing - original draft. **Karl Bane:** Validation, Writing - review & editing. **Derun Li:** Supervision. **Tianhuan Luo:** Validation. **Olusola Omolayo:** Resources, Validation. **Gregory Penn:** Validation, Writing - review & editing. **Stefano De Santis:** Methodology, Validation. **Christoph Steier:** Project administration, Supervision. **Marco Venturini:** Methodology, Validation, Supervision, Writing - review & editing.

Declaration of competing interest

The authors declare that they have no known competing financial interests or personal relationships that could have appeared to influence the work reported in this paper.

Acknowledgment

We would like to thank Dr. Robert Warnock from SLAC, Rui Li from Jefferson Lab., Michael Borland, and Ryan Lindberg from Argonne National Lab. for their valuable suggestions during the study. We also would like to thank Alireza Nassiri and John Byrd for the discussion on the gasket models, Charles Hetzel, Timur Shaftan, and Alexei Blednykh from Brookhaven National Laboratory for the test of the bellows.

This work was supported by the U.S. Department of Energy under Contract No. DE-AC02-05CH11231.

Appendix A

A.1. Yokoya factors for elliptical chambers

The dipole chamber in the accumulator ring has an elliptical shape instead of round, with major axis $2a = 40$ mm and minor axis $2b = 14.2$ mm. The ratio of the impedance and wakefield between elliptical chamber and round chamber with a radius of b can be connected

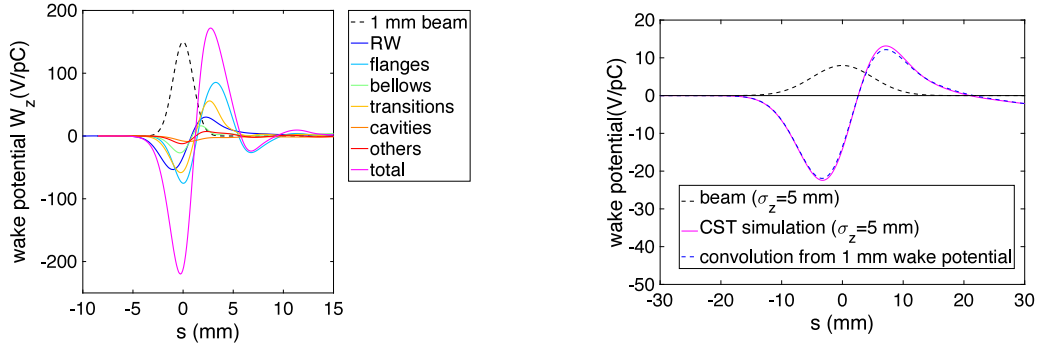


Fig. 20. Wake potential curve from a 1 mm beam in the AR: (a) pseudo-Green functions obtained by simulating a 1 mm beam in CST; (b) comparison between the convolution (blue curve), generated by the total result in (a) with 5 mm Gaussian beam, and the CST result directly driven by 5 mm beam (magenta curve).

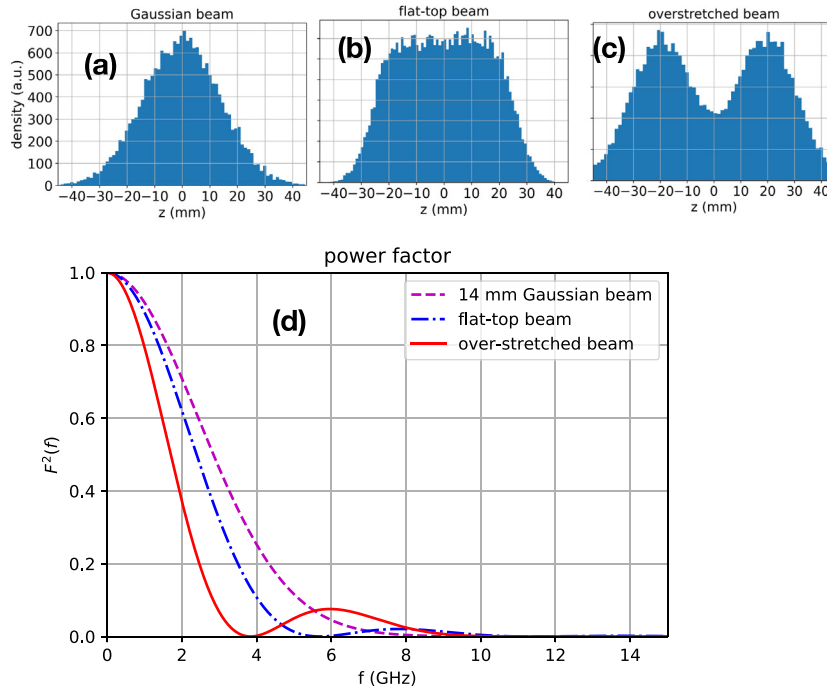


Fig. 21. Beam distributions of (a) a rms. 14 mm Gaussian beam, (b) a flat-top beam with rms. bunch length 14 mm and (c) a overstretched double-horn beam in the SR. (d) frequency spectrum of the different distributions.

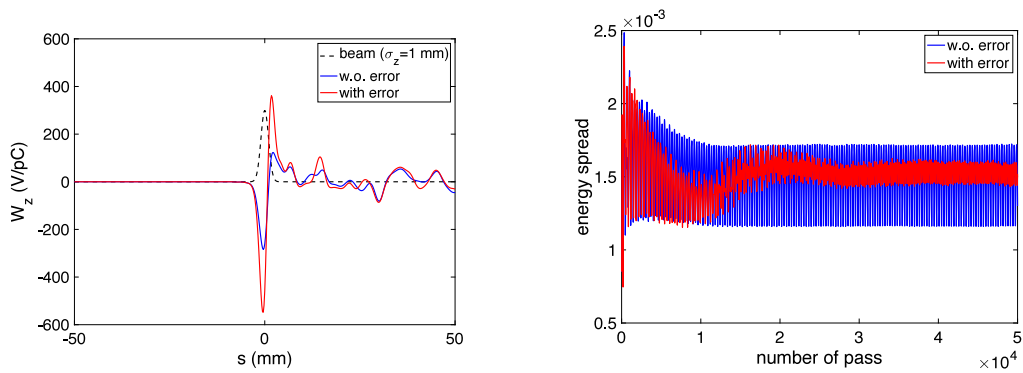


Fig. 22. Error analysis of impedance budget. Left: comparison of pseudo-Green function with and without weldment errors. Right: Corresponding beam dynamics study with error and without error, specifically for the evolution of the energy spread for a 4 nC beam in the storage ring without high harmonic cavities. Errors from weldment have the effect of instability suppression due to the conductance of the impedance.

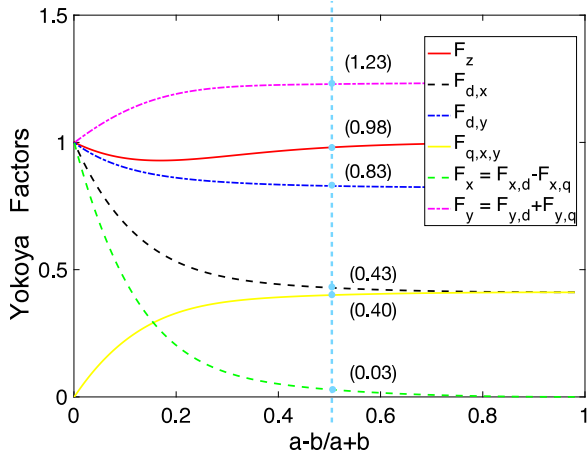


Fig. A.23. Yokoya factors depending on the ratio of $a - b/a + b$.

with Yokoya factors [28], which is given as a function of the elliptic parameter u_0 by:

$$\frac{a-b}{a+b} = e^{-2u_0}$$

$$F_z(u_0) = \frac{\sinh(u_0)}{2\pi} \int_0^{2\pi} dv \frac{Q_0^2(v, u_0)}{\sqrt{\sinh^2(u_0) + \sin^2(u_0)}} \quad (\text{A.1})$$

$$F_{x,d}(u_0) = \frac{\sinh^3(u_0)}{4\pi} \int_0^{2\pi} dv \frac{Q_{1x}^2(v, u_0)}{\sqrt{\sinh^2(u_0) + \sin^2(u_0)}}$$

$$F_{y,d}(u_0) = \frac{\sinh^3(u_0)}{4\pi} \int_0^{2\pi} dv \frac{Q_{1y}^2(v, u_0)}{\sqrt{\sinh^2(u_0) + \sin^2(u_0)}}$$

$$F_q(u_0) = \frac{\sinh^3(u_0)}{4\pi} \int_0^{2\pi} dv \frac{Q_0 Q_{xy}(v, u_0)}{\sqrt{\sinh^2(u_0) + \sin^2(u_0)}}$$

with:

$$Q_0(v, u_0) = 1 + 2 \sum_{m=1}^{\infty} (-1)^m \frac{\cos 2mv}{\cosh 2mu_0} \quad (\text{A.2})$$

$$Q_{1x}(v, u_0) = 2 \sum_{m=0}^{\infty} (-1)^m (2m+1) \frac{\cos(2m+1)v}{\cosh(2m+1)u_0}$$

$$Q_{1y}(v, u_0) = 2 \sum_{m=0}^{\infty} (-1)^m (2m+1) \frac{\cos(2m+1)v}{\cosh(2m+1)u_0}$$

$$Q_{xy}(v, u_0) = -8 \sum_{m=0}^{\infty} (-1)^m \frac{m^2 \cos(2mv)}{\cosh(2mu_0)}$$

For $(a-b)/(a+b) > 0.5$, the Yokoya factors approach asymptotic limits, as shown in Fig. A.23. For the AR dipole chamber, $a-b/a+b = 0.48$, yielding the following Yokoya factors: longitudinal, $F_z = 0.98$; horizontal dipolar $F_{d,x} = 0.43$; vertical dipolar $F_{d,y} = 0.83$; and quadrupolar $F_q = 0.40$, which is defocusing in the Y direction and focusing in the X direction.

Appendix B. Resistive wall impedance for parallel plates

The most significant plate geometries in the storage ring are the kicker and in-vacuum undulators (IVUs) in the straight sections. Since they contribute the most narrow gap in the vertical plane and are relatively long, they contribute significantly to both the vertical dipolar wakefield and the quadrupolar wakefield.

An accurate calculation of the wakefields for a flat geometry can be obtained analytically with the method of surface impedance [29]:

$$Z_l(\kappa) = 2 \left(\frac{Z_0 c}{4\pi} \right) \left(\frac{s_0}{ca^2} \right) \int_0^{\infty} dx \cdot \text{sech}(x) \quad (\text{B.1})$$

$$\times \left(\frac{2}{1-i} \frac{1}{\sqrt{\kappa}} \cosh(x) - i\kappa \frac{\sinh(x)}{x} \right)^{-1}$$

$$Z_{y,d}(k) = 2 \left(\frac{Z_0 c}{4\pi} \right) \left(\frac{2}{cka^3} \right) \int_0^{\infty} dx \cdot x^2 \frac{\text{csch}(x)}{\sinh(x)/\epsilon - ika \cosh(x)/x}$$

$$Z_{y,q}(k) = 2 \left(\frac{Z_0 c}{4\pi} \right) \left(\frac{2}{cka^3} \right) \int_0^{\infty} dx \cdot x^2 \frac{\text{sech}(x)}{\cosh(x)/\epsilon - ika \sinh(x)/x}$$

References

- [1] C. Steier, A. Anders, J. Byrd, K. Chow, S. De Santis, R. Duarte, J.-Y. Jung, T. Luo, H. Nishimura, T. Oliver, R+D Progress Towards a Diffraction Limited Upgrade of the ALS, Tech. rep., Lawrence Berkeley National Lab.(lbl), Berkeley, CA (United States), 2017.
- [2] C. Steier, P. Amstutz, K. Baptiste, P. Bong, E. Buice, P. Casey, K. Chow, R. Donahue, M. Ehrlichman, J. Harkins, et al., Design progress of ALS-U, the soft x-ray diffraction limited upgrade of the advanced light source, in: 10th Int. Particle Accelerator Conf.(IPAC'19), Melbourne, Australia, 2019.
- [3] M. Borland, et al., Progress toward an ultimate storage ring light source, J. Phys. Conf. Ser. 425 (4) (2013) 042016.
- [4] K.L. Bane, R.D. Ruth, Bunch lengthening calculations for the SLC damping rings, in: Proceedings of the 1989 IEEE Particle Accelerator Conference., 'Accelerator Science and Technology, IEEE, 1989, pp. 789–791.
- [5] K. Bane, Longitudinal stability study for the FACET-II e+ damping ring, 2016, arXiv preprint arXiv:1611.08042.
- [6] M.P. Sangroula, R.R. Lindberg, R.M. Lill, R. Zabel, Measuring vacuum component impedance for the argonne advanced photon source upgrade, Phys. Rev. Accel. Beams 23 (8) (2020) 082803.
- [7] V. Smaluk, Impedance computations and beam-based measurements: A problem of discrepancy, Nucl. Instrum. Methods Phys. Res. A 888 (2018) 22–30.
- [8] Y.-C. Chae, Y. Wang, Impedance database II for the advanced photon source storage ring, in: 2007 IEEE Particle Accelerator Conference, PAC, 2007, pp. 4336–4338.
- [9] R.R. Lindberg, Theory of coupled-bunch longitudinal instabilities in a storage ring for arbitrary rf potentials, Phys. Rev. Accel. Beams 21 (12) (2018) 124402.
- [10] A. Blednykh, G. Bassi, V. Smaluk, R. Lindberg, Impedance modeling and its application to the analysis of the collective effects, Phys. Rev. Accel. Beams 24 (2021) 104801.
- [11] A.W. Chao, Physics of Collective Beam Instabilities in High Energy Accelerators, Wiley, 1993.
- [12] P.B. Wilson, Introduction to Wakefields and Wake Potentials, Tech. Rep., SLAC-PUB-4547, 1989.
- [13] W. Panofsky, W. Wenzel, Some considerations concerning the transverse deflection of charged particles in radio-frequency fields, Rev. Sci. Instrum. 27 (11) (1956) 967.
- [14] B.W. Zotter, S.A. Kheifets, Impedances and Wakes in High-Energy Particle Accelerators, World Scientific, 1998.
- [15] M. Ehrlichman, T. Hellert, S. Leemann, G. Penn, C. Steier, C. Sun, M. Venturini, D. Wang, The three-dipole kicker injection scheme for the ALS-U accumulator ring, 2021, arXiv preprint arXiv:2106.08516.
- [16] R.R. Lindberg, Stabilizing effects of chromaticity and synchrotron emission on coupled-bunch transverse dynamics in storage rings, Phys. Rev. Accel. Beams 24 (2) (2021) 024402.
- [17] S. Persichelli, J.M. Byrd, S.D. Santis, D. Li, T. Luo, J. Osborn, C.A. Swenson, M. Venturini, Y. Yang, A preliminary beam impedance model of the advanced light source upgrade at LBL, in: NAPAC2016, Chicago, IL, USA, 2016.
- [18] D. Wang, K. Bane, D. Li, T. Luo, S. De Santis, M. Venturini, The broad-band impedance budget in the accumulator ring of ALS-U project, in: Proc. NAPAC'19, 2019, pp. 74–77, <http://dx.doi.org/10.18429/JACoW-NAPAC2019-MOZBA6>.
- [19] K.L. Bane, T. Naito, T. Okugi, Q. Qin, J. Urakawa, Impedance analysis of bunch length measurements at the ATF damping ring, Int. J. Appl. Electromagn. Mech. 14 (1–4) (2002) 197–202.
- [20] M. Borland, T. Berenc, User's manual for elegant, 2021.
- [21] P. He, et al., Accelerator vacuum technology challenges for next-generation synchrotron-light sources, in: 8th Int. Particle Accelerator Conf.(IPAC'17), Copenhagen, Denmark, 14–19 May, 2017, JACOW, Geneva, Switzerland, 2017, pp. 4830–4835.
- [22] S. Calatroni, P. Chiggiato, P.C. Pinto, M. Taborelli, M. Grabski, J. Ahlbäck, E. Al-Dmour, P.F. Tavares, NEG thin film coating development for the MAX IV vacuum system, in: Proc. 4th Int. Particle Accelerator Conf., IPAC'13, 2013, pp. 3385–3387.
- [23] R. Nagaoka, Impedance and Instabilities of Low Gap Chambers, Tech. Rep., Synchrotron SOLEIL, 2019.

- [24] M. Migliorati, E. Belli, M. Zobov, Impact of the resistive wall impedance on beam dynamics in the future circular e+e- collider, *Phys. Rev. Accel. Beams* 21 (4) (2018) <http://dx.doi.org/10.1103/physrevaccelbeams.21.041001>.
- [25] Computer simulation technology, CST particle studio, 2021, URL <http://www.cst.com/Products/CSTPS>.
- [26] T. Weiland, CST User Manual, CST, 2018.
- [27] A.W. Chao, K.H. Mess, et al., *Handbook of Accelerator Physics and Engineering*, World Scientific, 2013.
- [28] K. Yokoya, Resistive wall wake function for arbitrary pipe cross section, in: *Proceedings of International Conference on Particle Accelerators*, IEEE, 1993, pp. 3441–3443.
- [29] K. Bane, G. Stupakov, Using surface impedance for calculating wakefields in flat geometry, *Phys. Rev. Spec. Top. Accel. Beams* 18 (3) (2015) <http://dx.doi.org/10.1103/physrevstab.18.034401>.
- [30] K. Bane, M. Sands, Wake fields of very short bunches in an accelerating cavity, *Part. Accel.* 25 (SLAC-PUB-4441) (1987) 73.
- [31] L. Palumbo, V.G. Vaccaro, M. Zobov, Wake fields and impedance, 2003, arXiv preprint [Physics/0309023](https://arxiv.org/abs/Physics/0309023).
- [32] G. Stupakov, Low frequency impedance of tapered transitions with arbitrary cross sections, *Phys. Rev. Spec. Top. Accel. Beams* 10 (9) (2007) 094401.
- [33] V. Smaluk, R. Fielder, A. Blednykh, G. Rehm, R. Bartolini, Coupling impedance of an in-vacuum undulator: Measurement, simulation, and analytical estimation, *Phys. Rev. Spec. Top. Accel. Beams* 17 (7) (2014) 074402.
- [34] B. Podobedov, S. Krinsky, Transverse impedance of tapered transitions with elliptical cross section, *Phys. Rev. Spec. Top. Accel. Beams* 10 (7) (2007) 074402.
- [35] Y.T. Huang, C.M. Cheng, Y.C. Yang, C.K. Chan, C.C. Chang, Preliminary design of rf-shielded bellows, in: *IPAC2019*, 2019.
- [36] H. Hseuh, SR chambers & RF bellows, in: *ASAC Review*, 2009.
- [37] F. Zimmermann, Impedance of flanges, in: *RLC Meeting*, 2005.
- [38] A. Blednykh, B. Bacha, G. Bassi, C. Hetzel, B. Kosciuk, V. Smaluk, T. Shaftan, G. Wang, Impedance of the flange joints with the rf contact spring in nsls-II, in: *IPAC2019*, Melbourne, Australia, 2019.
- [39] CF-RFF gaskets, 2021, URL <https://www.atlasuhv.com/products/all-metal-uhv-seals-gaskets/copper-cf-rf-flare-gaskets/>.
- [40] R. Holtzapple, M. Billing, D. Hartill, W. Stedinger, B. Podobedov, Streak camera measurements of the longitudinal distribution of a single bunch in CESR, in: *Proceedings of the 1999 Particle Accelerator Conference (Cat. No. 99CH36366)*, Vol. 5, IEEE, 1999, pp. 2978–2980.
- [41] D. Boussard, Report LABII/RF/int/75-2, 1975, CERN, Geneva, Switzerland.
- [42] K. Bane, E. Mahner, M. Benedikt, U. Wienands, A. Grudiev, G. Stupakov, Impedance considerations for the design of the vacuum system of the CERN PS2 proton synchrotron, in: *Conf. Proc.*, Vol. 100523, (SLAC-PUB-14158) 2010, MOPD017.
- [43] K. Oide, K. Yokoya, Longitudinal Single-Bunch Instability in Electron Storage Rings, *Tech. Rep.*, KEK, 1990.
- [44] A. Blednykh, A numerical study of the microwave instability at APS, in: *NAPAC16*, 2016, pp. p602–604.
- [45] Y. Cai, J. Flanagan, H. Fukuma, Y. Funakoshi, T. Ieiri, K. Ohmi, K. Oide, Y. Suetsugu, J. Rorie, Potential-well distortion, microwave instability, and their effects with colliding beams at KEKB, *Phys. Rev. Spec. Top. Accel. Beams* 12 (6) (2009) 061002.
- [46] E. Shaposhnikova, Signatures of microwave instability, in: *Beam Measurement*, World Scientific, 1999, pp. 351–377.
- [47] K. Satoh, Y. Chin, Transverse mode coupling in a bunched beam, *Nucl. Instrum. Methods Phys. Res.* 207 (3) (1983) 309–320.
- [48] G. Besnier, D. Brandt, B.W. Zotter, The transverse mode coupling instability in large storage rings, *Part. Accel.* 17 (CERN-LEP-TH-84-11) (1984) 51–77.
- [49] V. Balbekov, Transverse mode coupling instability threshold with space charge and different wakefields, *Phys. Rev. Accel. Beams* 20 (3) (2017) 034401.
- [50] R. Warnock, K. Bane, Numerical solution of the Haïssinski equation for the equilibrium state of a stored electron beam, *Phys. Rev. Accel. Beams* 21 (12) (2018) 124401.
- [51] W.-H. Cheng, A.M. Sessler, J.S. Wurtele, Varying chromaticity: A damping mechanism for the transverse head-tail instability, *Phys. Rev. E* 56 (4) (1997) 4695.
- [52] Y.H. Chin, A.W. Chao, M.M. Blaskiewicz, Y. Shobuda, Chromaticity effects on head-tail instabilities for broadband impedance using two particle model, Vlasov analysis, and simulations, *Phys. Rev. Accel. Beams* 20 (7) (2017) <http://dx.doi.org/10.1103/physrevaccelbeams.20.071003>.
- [53] M. Venturini, Passive higher-harmonic rf cavities with general settings and multibunch instabilities in electron storage rings, *Phys. Rev. Accel. Beams* 21 (2018) 114404, <http://dx.doi.org/10.1103/PhysRevAccelBeams.21.114404>, URL <https://link.aps.org/doi/10.1103/PhysRevAccelBeams.21.114404>.
- [54] S. Myers, Stabilization of the Fast Head-Tail Instability by Feedback, *Tech. Rep.*, CERN-LEP-RF/87-28, 1987.
- [55] S. Kurennoy, Pumping Slots: Coupling Impedance Calculations and Estimates, *Tech. Rep.*, Superconducting Super Collider Lab, 1993.
- [56] Time-domain solver for transient response to driven fields and beam excitations of wakefields, 2021, URL https://portal.slac.stanford.edu/sites/ard_public/acd/Pages/t3p.aspx.
- [57] M. Venturini, Passive higher-harmonic rf cavities with general settings and multibunch instabilities in electron storage rings, *Phys. Rev. Accel. Beams* 21 (11) (2018) 114404.
- [58] R.R. Lindberg, Experimental advanced photon source upgrade project: verification of the world's leading hard X-ray light source impedance modeling for next-generation light sources, in: *Beam Tests and Commissioning of Low Emittance Storage Rings Workshop*, *Tech. Rep.*, Argonne National Laboratory, 2019.